

# Optomechanical backaction processes in a bulk rare-earth doped crystal

A. Louchet-Chauvet,<sup>1,2,\*</sup> P. Verlot,<sup>3,4</sup> J.-P. Poizat,<sup>5</sup> and T. Chanelière<sup>5</sup>

<sup>1</sup>*ESPCI Paris, Université PSL, CNRS, Institut Langevin, 75005 Paris, France*

<sup>2</sup>*Université Paris-Saclay, CNRS, Laboratoire Aimé Cotton, 91400 Orsay, France*

<sup>3</sup>*Institut Universitaire de France, 1 rue Descartes, 75231 Paris, France*

<sup>4</sup>*Université Claude Bernard Lyon 1, 69622, Villeurbanne, France*

<sup>5</sup>*Univ. Grenoble Alpes, CNRS, Grenoble INP, Institut Néel, 38000 Grenoble, France*

We investigate a novel hybrid system composed of an ensemble of room temperature rare-earth ions embedded in a bulk crystal, intrinsically coupled to internal strain via the surrounding crystal field. We evidence the generation of a mechanical response under resonant light excitation. Thanks to an ultra-sensitive time- and space-resolved photodeflection setup, we interpret this motion as the sum of two resonant optomechanical backaction processes: a conservative, piezoscopic process induced by the optical excitation of a well-defined electronic configuration, and a dissipative, non-radiative photothermal process related to the phonons generated throughout the atomic population relaxation. Parasitic heating processes, namely off-resonant dissipative contributions, are absent. This work demonstrates an unprecedented level of control of the conservative and dissipative relative parts of the optomechanical backaction, confirming the potential of rare-earth-based systems as promising hybrid mechanical systems.

## I. INTRODUCTION

Hybrid mechanical systems, consisting of a mechanical oscillator coupled to a quantum degree of freedom, have been identified as a promising tool to prepare, detect and manipulate non-classical macroscopic states of mechanical motion [1]. Hybrid mechanical coupling can be provided notably by electrostatic interaction between a resonator and a charge qubit [2], magnetic coupling with a spin qubit [3, 4], or strain-induced coupling with a qubit embedded in a solid [5–7]. Light-mediated coupling can also be achieved by placing a cloud of cold atoms in the optical lattice created by the reflection of a laser beam on a vibrating membrane [8]. Among these various approaches, the strain-induced coupling is particularly attractive because it intrinsically enables the design of monolithic devices exhibiting mechanical and thermal stability together with scalability. Yet, this advantage comes at a price: it can be difficult to design a hybrid strain-coupled architecture combining an excellent isolation of the optical emitter from its environment to allow its coherent manipulation, and a large sensitivity to mechanical motion. Various hybrid designs based on strain coupling have been proposed, where the quantum emitter is based either on a single system, namely a quantum dot [5], a nitrogen-vacancy center in diamond [7], or on an ensemble of rare-earth ions in a crystal [9, 10].

The first step towards full control of the optomechanical interaction in a strain-coupled hybrid system consists in investigating the sensitivity of the quantum system to an applied strain or pressure by measuring the induced detuning of the atomic resonance [11–13]. Aside from quantum optomechanics, this so-called piezospectroscopic effect offers interesting applications as a sensi-

tive strain probe in bulk materials [14–16] or heterostructures [17].

Further control of a hybrid system requires the exploration of the associated counterpart *ie* the backaction effect: generating strain or motion by addressing the quantum states of the atomic system, typically using optical excitation [18]. We shall refer to this as the *piezoscopic* effect. An example of this very fundamental mechanism can be observed when an atom or ion changes its apparent size due to the promotion of the outer electron in a higher energy level. This change of size is particularly spectacular in Rydberg atoms where the principal quantum number can reach large values, leading to significant atomic size variations [19]. Demonstrating this piezoscopic effect is notoriously challenging because of the unavoidable presence of dissipative optical processes that may ultimately result in photothermal contributions to the optically-induced motion [20, 21]. For example, in ultra-sensitive cavity optomechanical systems, these are often uncontrolled and attributed to residual, off-resonant absorption processes [22], eventually leading to a net decrease of quantum optomechanical correlations at the output of the system [23]. While having been little discussed, this problematic is also relevant to hybrid mechanical systems, where the quantum compound may dissipate heat via non-radiative processes following optical excitation.

In this work, we demonstrate the generation of mechanical motion following optical excitation in a novel strain-coupled hybrid mechanical system based on a large ensemble of ions embedded in a cm-scale monocrystal. The absence of sharp mechanical resonances in such a system enables full temporal and spatial reconstruction of the optically induced motion. Our demonstration relies on an ultra-sensitive time-resolved optomechanical tomography setup. This allows us to unambiguously address the photothermal and piezoscopic contributions to the resulting driven displacement. We also verify the res-

---

\* anne.louchet-chauvet@espci.fr

onant nature of relative contributions with respect to the atomic optical line, confirming their fundamental connection with the internal dynamics of the atomic system. The absence of a parasitic, non-resonant photothermal effect is remarkable in these materials. In particular, the photothermal component is fully described by the non-radiative relaxation dynamics of the ions, in contrast with most optomechanical systems so far, which generally argue upon parasitic, off-resonant absorption processes. Overall the degree of understanding and control of both the conservative and dissipative part of the optomechanical backaction confirms the potential of rare-earth-based systems as hybrid optomechanical systems.

## II. OPTOMECHANICAL TRANSDUCTION IN Tm:YAG

### A. Rare-earth doped crystals and Tm:YAG

In a rare-earth ion-doped crystal, optical transitions within the  $4f$  configuration are shielded from environment perturbations by the outer  $5s$  and  $5p$  electrons. Due to this shielding, the rare earth ions can exhibit very long population and coherence lifetimes at cryogenic temperature [24]. This motivates the development of many quantum technology architectures leading to state-of-the-art quantum storage [25], laser stabilization [26], noise-free microwave to optical conversion [27], or more recently quantum computing [28]. Among the rare-earth-doped crystals, Tm:YAG combines a long optical coherence lifetime [29], long-lived storage states [30], and a laser diode-accessible optical transition. Several quantum memory schemes have been proposed in this crystal [31, 32]. It is also at the heart of several wideband radiofrequency signal processing architectures, relying on the large static inhomogeneous broadening of the optical line [33–35].

The sensitivity of optical lines to strain in a rare-earth doped crystal via a distortion of the crystal has been known for a long time and has been used to further characterize the insertion site of the rare-earth impurity [36]. The converse, piezoscopic effect, associated to the promotion of a rare-earth ion to an excited electronic state, is by far more elusive. Indeed, the absorption of optical excitation leads to resonant photothermal effects, generally triggered on purpose to analyze the non-radiative processes [37, 38]. In addition, the effective shape of the ion is expected to be dominated by the shielding electrons, literally screening the modification of the optically active  $4f$  electronic orbitals.

The experimental challenge of observing the piezoscopic effect in rare-earth ion-doped crystals can be facilitated by addressing a large ensemble of identical ions without lessening its interest for quantum optomechanics. However, at cryogenic temperatures, their excellent coherence properties lead to frequency-selective behaviour [24], limiting the expected enhancement. At room temperature, on the other hand, the frequency-

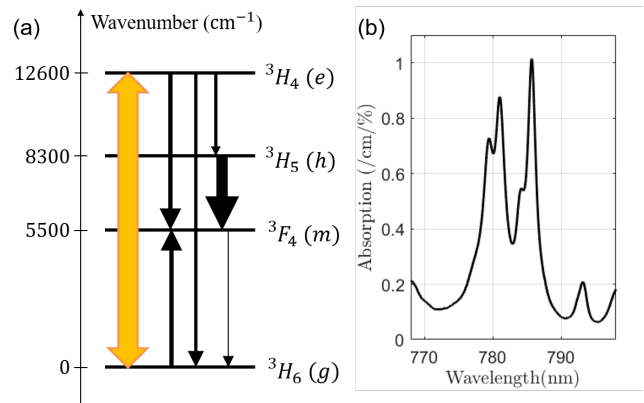


FIG. 1. (a) Simplified Tm:YAG level system and main relaxation mechanisms. Each horizontal line represents a Stark multiplet, referred to as either its spectroscopic term such as  $^3H_4$  or a letter such as  $e$ . Optical excitation (double arrow) promotes Tm ions to the excited level. The main relaxation mechanisms are depicted with single arrows. The thickness of the arrows symbolizes the magnitude of the relaxation rate. (b) Room-temperature absorption spectrum of Tm:YAG [43]. Each peak corresponds to a transition between a pair of  $^3H_6$  and  $^3H_4$  Stark sublevels.

selective behaviour disappears and all the ions contribute identically. The spectroscopic properties of room-temperature REIC have been well documented, motivated by the development of solid-state lasers [39]. Tm:YAG is no exception [40] thanks to its central role in the development of  $2\ \mu\text{m}$  lasers [41]. For the same reason, the quality of Czochralski-grown oxides has made significant progress over the past 40 years and the quality of Tm:YAG monocrystals is now very good [42] precisely driven by the need of laser materials with low parasitic losses to avoid damages.

Transferring a sizeable fraction of  $\text{Tm}^{3+}$  ions within a large ensemble can be achieved by optically pumping into the so-called *metastable* state  $^3F_4$  which is commonly used as a shelving state for laser operation. Let us focus on the four Stark multiplets that take part in the laser operation  $^3H_6$ ,  $^3F_4$ ,  $^3H_5$  and  $^3H_4$ , respectively denoted as  $g$ ,  $m$ ,  $h$ , and  $e$  in the following. The four-level system is depicted in Figure 1, together with the room-temperature absorption spectrum around 780 nm. The crystal exhibits well-resolved lines reflecting the Stark multiplicity of the electronic levels. The strongest lines are found at 781 and 786 nm. Pumping Tm ions along one of these lines promotes them to the excited state  $e$ . From there they essentially decay into state  $m$ , partly cascading through the short-lived state  $h$ . When the doping concentration exceeds 1%, Tm-Tm cross-relaxation significantly contributes to populate level  $m$  [44]. This optical pumping scheme can lead to a significant fraction of a large Tm ensemble stored for a few ms in the metastable state  $m$ .

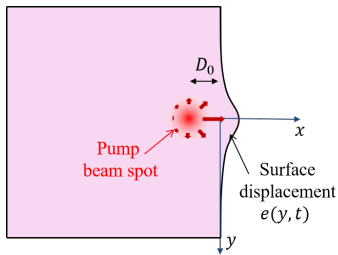


FIG. 2. Schematic optomechanical transduction principle in a bulk crystal. The pumping beam is sent in the  $z$  direction and focused close to an edge of the crystal. The optically induced volumic strain leads to a displacement field oriented preferentially towards the surface (solid arrows).

### B. Optomechanical backaction in a bulk material

In this section we describe our strategy to trigger an optomechanical transduction in a bulk Tm:YAG crystal and detect it optically.

Choosing to work in a bulk system encompasses several advantages. First, millimetric sample dimensions allow spatially-resolved optical characterization of the optomechanical response with conventional probe beam waists [45]. Second, the absence of sharp mechanical resonances (generally present in lower dimensional systems [4, 18]) enables a non-resonant, time-resolved study. Given the millisecond-scale population lifetime in our crystal, a direct measurement of the optomechanical response to a pulsed excitation is possible.

We consider a pump beam focused within a bulk, parallelepipedic Tm-doped YAG crystal. The beam is shined close to an edge of the crystal, such that the resulting strain field is mainly directed towards the surface and this way maximizes the corresponding surface distortion  $e(y, t)$  (see Figure 2). If the depth of field of the pump beam is much larger than the crystal thickness  $L_z$ , and if the absorption of the pump field is low, one can consider this surface distortion to be invariant along the  $z$  direction. The surface distortion  $e(y, t)$  is retrieved using the photodeflection technique, a non-interferometric method that allows to measure tilt angles of a reflective surface with sub- $\mu$ rad sensitivity with the help of an auxiliary probe beam at a very different color [46]. We consider the beam geometry represented in Figure 3. While the pump beam propagates in the  $z$  direction, the probe beam is sent in the horizontal plane  $(x, z)$  towards the vertical surface, with a  $45^\circ$  angle of incidence. When the surface is distorted, the probe beam is vertically deflected by an angle  $2\phi$ . The angle  $\phi$  corresponds to the local slope of the surface along the vertical direction  $\phi(y) = \partial e / \partial y$ . This deflection is measured with a quadrant photodetector.

As for a majority of quantum emitters, the relaxation process in Tm:YAG involves both radiative and non-radiative contributions, associated with the conservative and dissipative components of the optomechanical back-

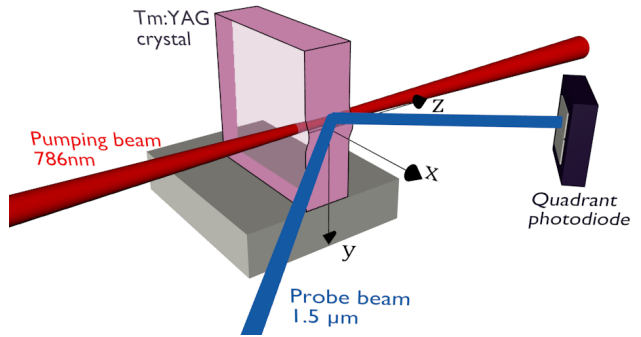


FIG. 3. Photodeflection setup geometry for the detection of an optomechanical backaction in a bulk medium. A pump beam is sent parallel to a crystal surface. A probe beam is reflected on this surface with a  $45^\circ$  angle of incidence. In the presence of an optomechanical transduction, the surface is distorted, leading to a vertical deflection of the reflected probe beam, captured by a quadrant photodetector.

action process, respectively. The former would be the aforementioned piezoscopic effect, that is the generation of strain resulting from the population transfer among different electronic states, whereas the latter would result from non-radiative decay mechanisms, also known as a photothermal effect. Disentangling these two contributions is a challenging problem since they are both resonant. Here, we take advantage of the bulk properties and study the time-dependent surface distortion in response to a rectangular light pulse. Because of the distinct time and space signatures associated with the piezoscopic and photothermal drives, this time-resolved optomechanical tomography method enables to unambiguously determine each of these contributions to the overall strain resulting from resonant pumping of the ions.

### C. Experimental results

We assemble an experimental setup according to the beam geometry described in the previous section (see Figures 2 and 3). More detail on the setup is given in Appendix A. The pump beam is temporally chopped into  $T_P = 3$  ms-long rectangular pulses sent with a 86 ms period. The transmitted pump beam intensity is initially attenuated by a factor  $e^{-\alpha L_z} \simeq 0.5$  according to the Beer-Lambert-Bouguer law, where  $\alpha = 2 \text{ cm}^{-1}$  is the absorption coefficient at the given wavelength of 786 nm and  $L_z = 4$  mm is the crystal length along the pump propagation direction. The transmitted intensity shown in Figure 4(a) slowly increases during the pulse, revealing the effective population pumping from the ground to the metastable state.

The principle of using time-resolved tomography for separating the conservative and dissipative contributions to the measured surface distortion is depicted in Figure 4(b). The time evolution of two photodeflection

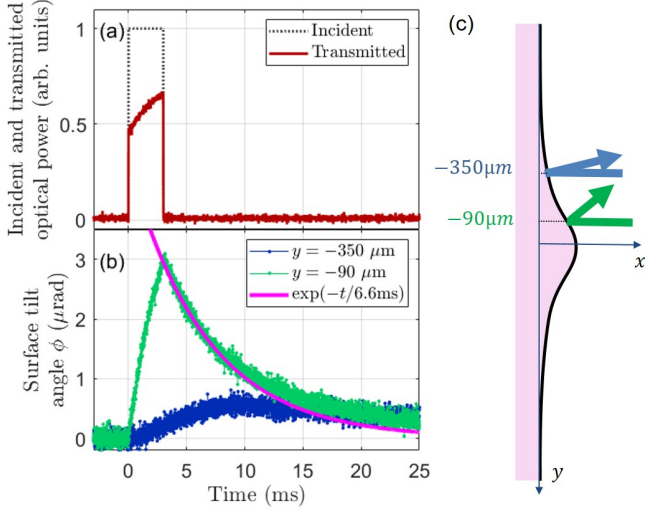


FIG. 4. (a) Incident and transmitted pumping laser light at 786 nm through our Tm:YAG crystal. The population transfer towards the metastable state leads to a slow increase in the transmitted light. (b) Surface tilt angle measured by photodeflection (averaged 128 times), for two relative positions of the pump and probe beam [schematically shown in (c)]. An exponential decay is also shown as a guide to the eye.

signals, acquired well apart on the crystal surface, are shown. When probed  $350 \mu\text{m}$  away from the pumping region (located at  $y = 0$ ), the surface tilt angle exhibits a damped response reaching  $0.6 \mu\text{rad}$  at its maximum, with a delay significantly larger than the pump pulse duration. This slow response strongly evokes the heat diffusion process occurring in the presence of a photothermal effect. On the other hand, when we probe the surface closer to the pumping position, we observe a steep response to the stepwise pumping, up to  $3 \mu\text{rad}$ , followed by a decay comparable with the metastable state lifetime. This is compatible with the expected instantaneous piezoscopic response that we will address in more detail in Sec. III A.

In order to unambiguously address both photothermal and piezoscopic contributions of the optomechanical backaction, we probe the surface of the crystal along the vertical direction by scanning the position  $y_i$  of the probe beam relative to the pumping position between  $-500$  and  $500 \mu\text{m}$ . This method enables point-by-point reconstruction of the surface shape along the  $y$  direction, with a spatial resolution given by the probe beam waist on the crystal surface ( $70 \mu\text{m}$  waist radius). The data is presented in Figure 5. We observe the rise and fall of a localized surface displacement, initially contained in a narrow region ( $|y| < 200 \mu\text{m}$ ), and spreading progressively after a few ms. This narrow feature is somewhat surprising as one would rather expect the surface bump to exhibit a width comparable to the depth of the pump beam  $D_0$  due to the broad angular distribution of the displacement field (see Figure 2). Actually the photodeflection measurement technique provides a particular sen-

sitivity to sharp features since the signal is proportional to the slope of the surface. The broad surface distortion may be present but we are unable to detect it. The presence of this narrow feature probably indicates a partial channelization of the observed displacement field along the crystalline axes. A complete description of the strain propagation mechanism in the crystal would require a specific study which is beyond the scope of the present paper.

We study the dependence of the photodeflection angle with respect to the excitation wavelength, over a  $781 - 795 \text{ nm}$  interval, covering four overlapping absorption lines between the Stark multiplets  $^3H_6$  and  $^3H_4$  (see Figure 1). The value of  $y$  is chosen such that the photodeflection signal is strongest ( $y = -90 \mu\text{m}$  at the bump side). In Figure 6 we plot the value of the deflection angle and observe that it closely follows the absorption coefficient as the pump wavelength is scanned, ruling out the possibility of a non-resonant contribution. It is also noticeable that the temporal variation of the photodeflection angle is unchanged over the whole wavelength range (see insets of Figure 6), indicating a preserved link between the optomechanical backaction and the internal atomic dynamics.

### III. MODELING THE OPTOMECHANICAL BACKACTION

In this section we model the piezoscopic and photothermal mechanisms in Tm:YAG. For each of them, we derive the surface distortion in the beam geometry used in our experiment, assuming translational invariance of the problem along the pumping beam direction  $z$ . By comparing the experimental data to the simulation results we are able to fully analyze the optomechanical backaction mechanism in our Tm:YAG system.

#### A. Piezoscopic surface displacement

We start by determining the spatio-temporal variations of the atomic populations excited by a pulsed pump beam with a gaussian profile. We describe the light-matter interaction with a rate-equation formalism (see Appendix B), and obtain the atomic populations dynamics in the four Tm levels (see Figure 7). Up to 60 % of the population reaches the metastable state in the center of the beam at the end of the pumping pulse.

Since the populations in levels  $e$  and  $h$  never exceed 5% in the center of the beam, we only focus on the piezoscopic effect triggered by the population transfer between levels  $g$  and  $m$ . For simplicity, we consider that the effect of this population transfer is a change of the ionic radius, defined as  $\xi = (r_m - r_g)/r_g$  where  $r_m, r_g$  refer to the ionic radii in the metastable and ground states respectively. We focus on the fraction of the displacement field exclusively oriented in the  $x$  direction, our photode-

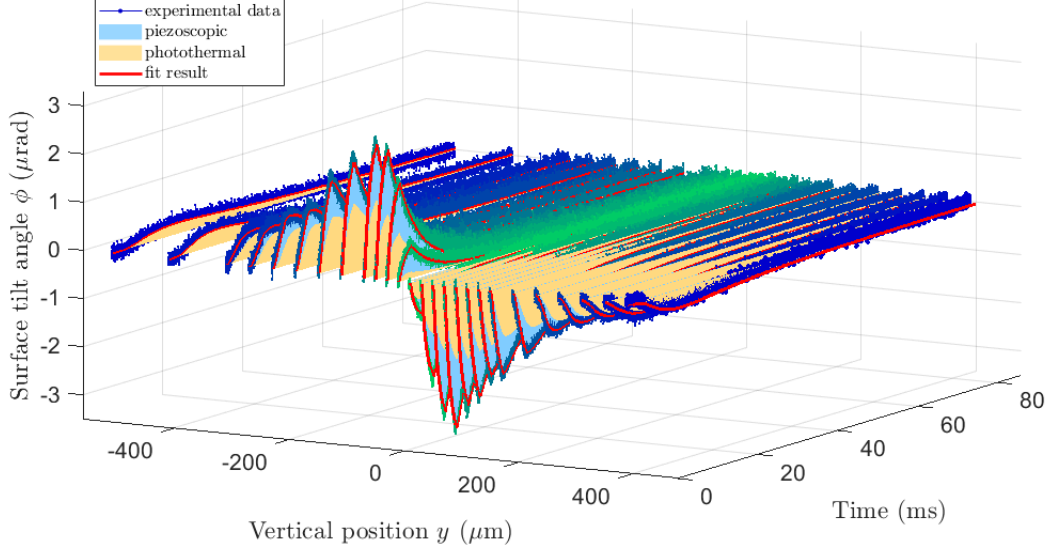


FIG. 5. Time-resolved tomography of the optomechanically distorted crystal surface. A 3 ms long, 786-nm wavelength pump pulse hits the crystal  $D_0 = 1.4$  mm away from the surface. The surface tilt angle  $\phi$  is measured for several values of the relative vertical positions  $y$  of the probe and pump beams. Each curve is the result of 128 averages. All the curves are offset to reach zero at long times. The filled areas correspond to the photothermal and piezoscopic contributions derived from the fit (see section III C).

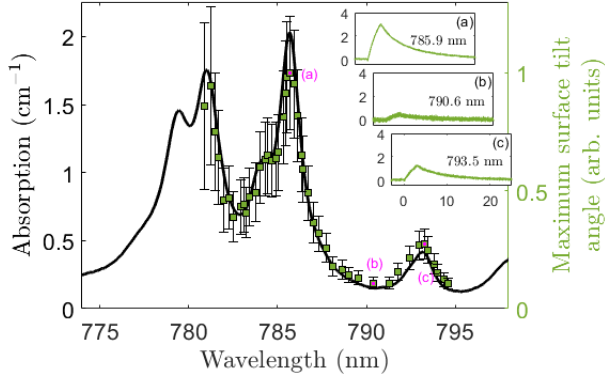


FIG. 6. Variation of the maximum surface tilt angle at the end of the pump pulse while the pump laser wavelength is scanned over a 781 – 795 nm interval (squares). The angle is normalized with respect to the pump power variations. On the same graph we plot the absorption coefficient 2%-doped Tm:YAG at room temperature (solid line) [43]. The three insets (a, b, c) show the similar time dependence of the normalized angle for three particular wavelengths.

flection technique being unidirectional as noted in section II C. We simply estimate the displacement  $e_{\text{piezo}}$  of the surface as the sum of the local deformation between the center of the pump beam and the surface:

$$e_{\text{piezo}}(y, t) = \sqrt[3]{n_{\text{Tm}}} 2r_g \xi \int_{-D_0}^0 n_m(x, y, t) dx \quad (1)$$

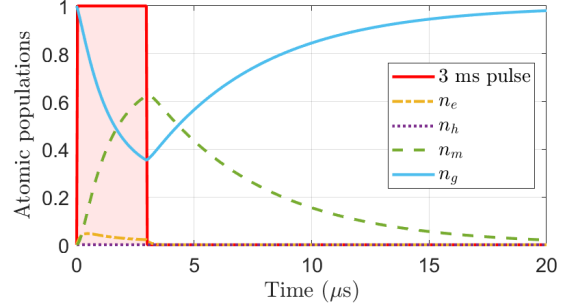


FIG. 7. Atomic populations in a room-temperature Tm:YAG 4-level system, at the center of a 230 mW pumping pulse focused on a  $22 \mu\text{m}$  waist spot. The pulse is rectangular and 3 ms long.

where  $n_{\text{Tm}}$  is the volumic density of Tm ions in the crystal, and  $n_m$  is the fractional population in the  $m$  state at position  $(x, y)$  and time  $t$ . The ionic radius of  $\text{Tm}^{3+}$  in the ground state ( $r_g = 0.994 \text{\AA}$ ) is found in [47]. Equation 1 reflects the instantaneous nature of the piezoscopic effect and its direct connection to the atomic population in the metastable state.

Given the separability of the time and space dependence of the atomic populations (see Appendix B), this expression simplifies to

$$e_{\text{piezo}}(y, t) = e_{\text{piezo}}(y, T_P) g_m(t) \quad (2)$$

where  $g_m(t)$  is the normalized time dependence of  $n_m(x, y, t)$ .



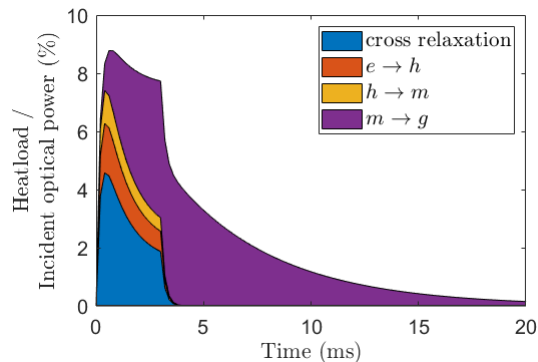


FIG. 8. Solid line: calculated heatload due to phonon emission triggered by a 3-ms rectangular pulse in a Tm:YAG crystal. The heatload power is normalized with respect to the incident power (230 mW in this calculation). The beam waist radius is 22  $\mu\text{m}$ . The heatload is calculated at the center of the pump beam and broken down into its 4 contributions.

### B. Photothermal surface displacement

We now describe the mechanical deformation associated with the heating contribution of the pumping pulse. As observed experimentally, we do not detect any parasitic, non-resonant contribution (see Figure 6) so we can focus exclusively on the heat generation linked to the phonons emitted throughout the atomic relaxation process. The modeling is done in two steps. First, we consider the population dynamics to estimate the non-radiative phonon contribution to heat using the parameters documented in the laser literature. Second, we solve the heat equation to obtain a thermal map (in space and time) during the experiment.

Several processes are involved. Each step of the decay of the Tm ions from the excited to the ground state is partly non-radiative and generates heat. In addition, in the cross-relaxation mechanism, phonons are produced to compensate for the detuning between the  $g \rightarrow m$  and the  $e \rightarrow m$  transitions [44]. Overall the total heatload power reads as a sum of four contributions depicted in Figure 8. Each of these contributions exhibits a time dependence related to the population evolution in the 4-level system (see Appendix C). Interestingly, the total heatload rapidly grows during the pulse and slowly decays after the end of the pulse. This persistence originates from the phonon generation along the  $m \rightarrow g$  decay path. This contribution is proportional to  $n_m(t)$ , which decays within a few ms.

The shortest timescale of the heatload variation is around  $\tau_{\text{heat}} = 1$  ms, leading to a corresponding thermal diffusion length  $L_{\text{diff}} = \sqrt{\alpha_{\text{diff}} \tau_{\text{heat}}} \simeq 60$   $\mu\text{m}$  (where  $\alpha_{\text{diff}} = 4 \times 10^{-6}$   $\text{m}^2 \cdot \text{s}^{-1}$  is the thermal diffusivity in YAG [48]). In a sample smaller than  $L_{\text{diff}}$ , the diffusion of such a heatload would be considered instantaneous. In a bulk monocrystal with millimetric dimensions however, the diffusion mechanism becomes prominent and must

therefore be taken into account for predicting the time-dependent temperature distribution. The latter is determined by solving the heat equation with the volumic heatload power as a time- and space-dependent source term (see Appendix D). This way we obtain the temperature distribution in the crystal volume  $T(x, y, t)$ .

The thermal expansion of the crystal in any direction is given by  $\kappa T$  where  $\kappa = 6.1 \times 10^{-6}$   $\text{K}^{-1}$  is the YAG linear thermal expansion coefficient. Finally, considering again only the displacement field directed towards the nearby surface, the displacement of the crystal surface due to the photothermal effect reads as:

$$e_{\text{therm}}(y, t) = \kappa \int_{-D_0}^0 dx T(x, y, t) \quad (3)$$

To sum up, besides being deeply linked to the internal dynamics of the Tm ions via the source term of the heat equation, the photothermal effect also reflects the diffusion mechanism that is bound to occur in a bulk sample through the time- and space-dependent temperature distribution.

### C. Surface displacement and photodeflection signal

In Figure 9 we plot the expected surface displacements  $e_{\text{piezo}}(y, t)$  and  $e_{\text{therm}}(y, t)$  provided by our two models described in sections III A and III B. Both effects give rise to a bump on the crystal surface, centered in  $y = 0$ . In the piezoscopic case, the bump exhibits a constant spatial width, while its time dependence is given by the metastable population evolution  $g_m(t)$  (see Eq. 2). The photothermal contribution, on the other hand, exhibits a progressive spatial broadening due to heat diffusion. In addition, its time evolution strongly depends on the value of  $y$ : the photothermal response is quasi-instantaneous on the center of the bump ( $y = 0$ ), closely resembling the piezoscopic response, but it is manifestly delayed away from the bump. The corresponding surface tilt angles  $\phi_{\text{piezo}}(y, t)$  and  $\phi_{\text{therm}}(y, t)$  are then obtained by deriving the displacements  $e_{\text{piezo}}(y, t)$  and  $e_{\text{therm}}(y, t)$  along the  $y$  dimension (see Appendix E).

We adjust the experimental surface tilt angles  $\phi_{\text{exp}}(y_i, t)$  measured at positions  $(y_i)$  with the following function:

$$\phi_{\text{exp}}(y_i, t) = \Phi_i(y_i) g_m(t) + \eta \phi_{\text{therm}}(y_i, t) \quad (4)$$

The first term corresponds to the piezoscopic effect whose time dependence  $g_m(t)$  is imposed by the metastable population evolution and whose space dependence  $\Phi_i(y_i)$  is left as a set of adjustable parameters. The second term is the photothermal contribution for which we allow only the multiplicative factor  $\eta$  to be adjustable.

The result is represented in the form of filled area plots in Figure 5. The good agreement with the experimental data demonstrates unequivocally that the photothermal effect on its own cannot explain the observed behaviour.

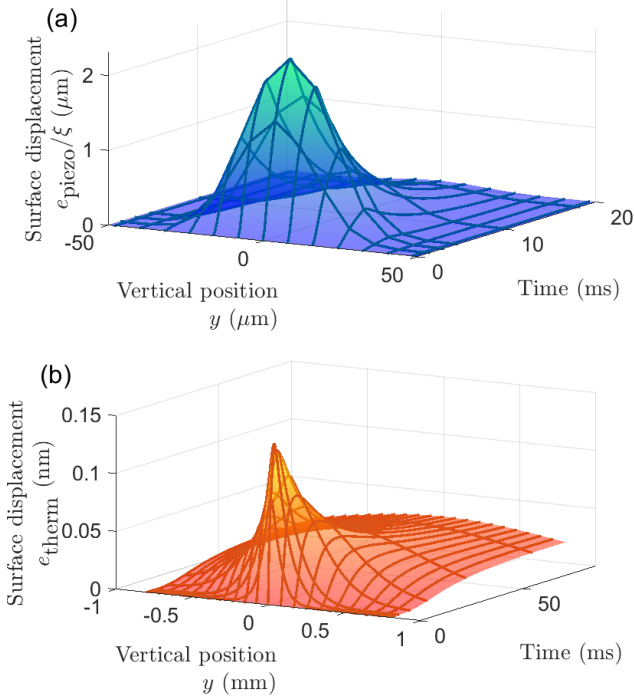


FIG. 9. Surface displacement for (a) the piezoscopic effect and (b) the photothermal effect as predicted by our two models, assuming a 3 ms pumping pulse. Note the different scales for the two graphs. For the piezoscopic effect we represent the surface displacement normalized by the fractional ionic radius change  $\xi$ .

It is the dominant contribution when probed at a long distance from the pump beam position ( $|y| > 300 \mu\text{m}$ ), but close to the center, the piezoscopic and photothermal effects are similar in size. The photothermal effect is slightly underestimated in our model but the order of magnitude is consistent ( $\eta = 2.6$ ).

## IV. DISCUSSION

### A. Focusing on the piezoscopic effect

Figure 10 shows the values of  $(\Phi_i)$  describing the piezoscopic contribution, as obtained from the fit described above. The data are well described by a Lorentzian-shaped surface displacement with a  $205 \mu\text{m}$  FWHM and a  $210 \text{ pm}$  amplitude at the end of the pumping pulse. This surface displacement is the result of the promotion of 60 % of about  $5 \cdot 10^{14} \text{ Tm}^{3+}$  ions in their metastable state.

Using the conservative nature of the piezoscopic effect, we can relate its magnitude using the pressure sensitivity of the Tm atomic line  $G_{\text{stress}} = \frac{\partial \omega}{\partial \sigma}$  (see Appendix F):

$$\Delta x = \hbar G_{\text{stress}} n_{\text{active}} n_{\text{Tm}} d_x \quad (5)$$

Applying this formula to our optically-pumped Tm:YAG

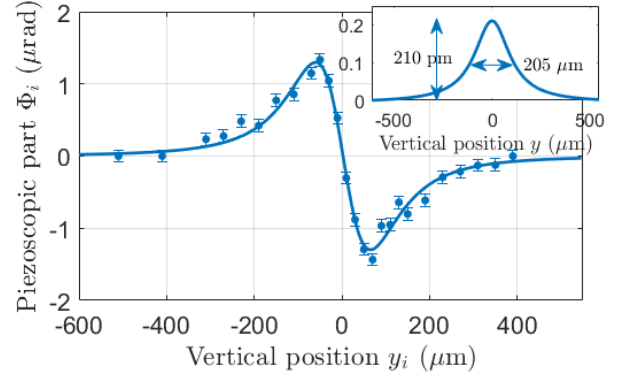


FIG. 10. Space dependence  $\Phi_i(y_i)$  (filled circles) of the piezoscopic contribution to the measured tilt angle as obtained from the fit by Eq. 4 (error bars are given by the fitting uncertainty on the parameter). A solid line corresponding to a lorentzian surface displacement reproduces well the data. Inset: lorentzian-shaped surface displacement inferred from the measured angles.

sample, we replace  $n_{\text{active}}$  by the metastable population at the end of the pump pulse, *ie* 60%. The exact value of  $G_{\text{stress}}$  is not known for the  ${}^3\text{H}_6 \rightarrow {}^3\text{F}_4$  transition in Tm:YAG, but a quick review shows that the pressure sensitivity lies between  $2\pi \times 40 \text{ Hz/Pa}$  and  $2\pi \times 300 \text{ Hz/Pa}$  for a broad range of host crystals, rare-earth dopants, and transitions. Choosing  $G_{\text{stress}} = 2\pi \times 68 \text{ Hz/Pa}$  as a characteristic value (as done in [16]) and setting  $d_x$  as the pump beam radius, we obtain an expected piezoscopic displacement  $\Delta x = 164 \text{ pm}$ , very close to the measured value ( $210 \text{ pm}$ ).

Full understanding and characterization the atomic origin of the piezoscopic effect is beyond the scope of this work, requiring accurate Hartree-Fock simulations of the Tm ion and the interaction of the crystal field with the  $4f$  electronic orbital shapes in the two relevant electronic states [49, 50]. Still, by comparing the experimental piezoscopically-driven surface displacement (Figure 10) to the one predicted by our model [Figure 9(a)], we are able to derive the fractional expansion of a single Tm ion along the  $g \rightarrow m$  transition, assuming a simple ionic radius dilation:  $\xi_{\text{exp}} \simeq 2 \cdot 10^{-4}$ . Our optomechanical setup provides a unique access to this parameter, that is obtained by considering only the observed macroscopic displacement field without an exact knowledge of the microscopic orbital shape change and the propagation of the strain field in the crystal.

### B. Perspectives

Comprehensive characterization of photothermal effects is generally difficult in hybrid systems, especially in micro- and nano-structures for which thermal actuation processes largely depend on defects and asymmetries [18, 51, 52], therefore being generally unpredictable.

Our time-resolved optomechanical tomography scheme, combined with a suitable sample geometry, enables us to shed a new light on photothermal motion as a fundamental hybrid optomechanical process. This backaction contribution is directly linked to the non-radiative relaxation mechanisms of the quantum emitter, and quantitatively relates to the internal atomic dynamics. This strong fundamental link between the atomic populations and the optomechanical backaction paves the way towards probing the internal dynamics of the hybrid system through its optomechanical response.

Moving further towards quantum hybrid rare-earth-based optomechanical systems requires operating at liquid helium temperatures or below, where coherent quantum state manipulation becomes possible [53, 54]. In this regime, the optical transitions are generally buried within a broad inhomogeneous absorption line, preventing direct coherent control. This issue is however routinely addressed either by isolating a narrow spectral subset of ions via spectral hole burning [55], or by rephasing techniques such as photon echo whose precision has been boosted recently in the quest towards quantum storage [56, 57]. Applying these techniques to mechanically engineered rare-earth materials (e.g. phononic structures [58]) therefore raises the realistic perspective of a new kind of efficient quantum hybrid transducers, with strong implications for quantum technologies [1, 59].

Finally, rare-earth ion-doped crystals offer an unprecedented level of control that may be very attractive in the field of optomechanics. Indeed, in these materials, the relaxation mechanisms strongly depend on the quantum states used, the nature of the ion and its environment. One can imagine addressing other transitions in a given crystal, considering various ion-host combinations [24], or even codoped samples [60, 61], to tune the optomechanical response. In particular, ytterbium-doped  $\text{YLiF}_4$  represents a key material thanks to its minimal number of non-radiative decay channels. This property, already exploited in the context of laser cooling of solids [62, 63], would also make this material an interesting candidate for solid-state laser-cooled, conservative optomechanics.

## V. CONCLUSION

In this work we have considered a hybrid system composed of a collection of around  $5 \cdot 10^{14}$  identical rare earth ions embedded in a bulk crystal, and coupled to internal strain. We have evidenced the generation of a mechanical response within this hybrid system under resonant light excitation, that we find to correspond to the sum of two optomechanical backaction processes: a conservative process related to the geometric shape change of the electronic orbitals (piezoscopic effect), and a dissipative process related to the phonons generated throughout the atomic relaxation (photothermal effect). The resonant nature of the two effects and their connection to the internal atomic state dynamics was confirmed. This

demonstration was performed at room temperature but could in principle be transposed to cryogenic temperatures where rare-earth ion-doped crystals exhibit exceptional coherence properties.

A hybrid system generally couples a mechanical degree of freedom to a quantum emitter exhibiting both radiative and non-radiative relaxation mechanisms. This work shows for the first time the inseparable nature of these two mechanisms. This approach sheds new light on hybrid systems and on the comprehension of non-conservative relaxation mechanisms to determine their fundamental quantum limits. It also paves the way towards a yet unexplored hybrid optomechanics paradigm, where the inevitable photothermal effects are not only comprehensively understood, but tunable to a certain extent. This work confirms the high potential of rare-earth-based systems in the swarming field of quantum technologies.

## ACKNOWLEDGMENTS

The authors are indebted to Jean-Louis Le Gouët and Ludovic Bellon for helpful discussions. The authors acknowledge support from the French National Research Agency (ANR) projects ATRAP (ANR-19-CE24-0008), and MIRESPIN (ANR-19-CE47-0011), and the LABEX WIFI (Laboratory of Excellence within the French Program "Investments for the Future") under references ANR-10-LABX-24 and ANR-10-IDEX-0001-02 PSL\*.

## Appendix A: Experimental details

The sample under study is a commercial YAG ( $\text{Y}_3\text{Al}_5\text{O}_{12}$ ) monocrystal (Scientific Materials) where  $\text{Tm}^{3+}$  ions substitute 2% of the  $\text{Y}^{3+}$  ions. It is a  $4 \times 10 \times 10$  mm parallelepiped, polished on all 6 faces. The crystal sits on top of a piece of aluminum, and contacted with a thin layer of thermal paste. The rest of the crystal is in contact with air. A 230 mW pump beam is focused on a  $22 \mu\text{m}$  waist radius spot inside the crystal, entering the  $10 \times 10$  surface of the crystal with normal incidence. The associated depth of focus is 4 mm, matching the crystal length along the pump beam propagation axis. The 2% doping ratio leads to a thulium volumic density of  $n_{\text{Tm}} = 2.76 \times 10^{20} \text{ cm}^{-3}$ . The number of ions addressed by this pump beam is of the order of  $5 \times 10^{14}$ . A photodiode records the transmitted light, and yields an experimental value for the pumping rate  $R$  subsequently used in the rate equation model.

The pump beam is a generated by a Toptica DLPro extended cavity diode laser, injected into a Toptica BoosTA 1V1 tapered amplifier. The laser is coarsely tunable over tens of nm around 785 nm by adjusting the position of the grating. The amplifier is actually optimized for 793 nm operation and its 3 dB bandwidth is limited to a few nm. Therefore the optical power at the output of the amplifier



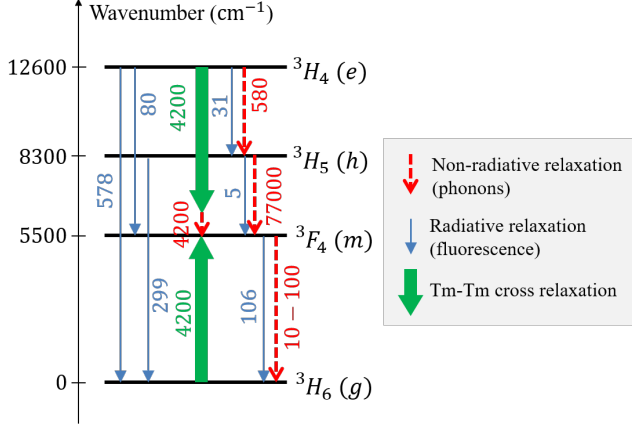


FIG. 11. Tm:YAG level system and relaxation mechanisms. Each Stark multiplet may be referred to as either its spectroscopic term (e.g.  $^3H_4$ ) or a letter (e.g. "e"). The vertically oriented numbers correspond to the relaxation rates (in  $s^{-1}$ ) inferred from references [40] and [64], assuming a 2% Tm doping rate. The non-radiative relaxation rate from  $m$  to  $g$  according to [40] is  $10 s^{-1}$ , but we extend it to  $100 s^{-1}$  in our model so that the metastable state lifetime matches the one measured in our sample (5 ms).

drops by a factor of 5 when the wavelength is varied from 793 to 781 nm. The beam is temporally shaped with an AA Opto-Electronic MT110 acousto-optic modulator.

The probe beam is provided by a Nettest Tunics external cavity diode laser emitting a few mW at a completely

different color (1550 nm), focused on the crystal distorted surface with a  $70 \mu m$  waist radius. The reflected beam is then collimated and directed towards the center of a Thorlabs PDQ30C quadrant photodiode with 150 kHz bandwidth. The quadrant photodiode signal is filtered via a DC-block and averaged over 128 shots to filter out slow technical noise due for example to air turbulence in the lab.

In the time-resolved tomography experiment (Figure 5), the parameter  $y$  is varied by vertically shifting the lens focusing the pump beam on the crystal, with the help of a manual linear translation stage.

## Appendix B: Rate equation modeling of the population evolution in Tm:YAG

The complete relaxation mechanisms at room temperature in the Tm four-level system are represented in Figure 11. The relevant parameters were found in references [40] and [64]. The excitation along the  $g \rightarrow e$  transition is represented by a time- and space-dependent pumping rate  $R$ , proportional to the optical irradiance. The pumping rate is derived experimentally from the measurement of the transmitted pump power (see Figure 4(a)). As an example, a 230 mW pump pulse focused on a  $22 \mu m$  waist radius corresponds to a  $R = 340 s^{-1}$  pumping rate along the  $g \rightarrow e$  transition during the pumping pulse. We model the population dynamics with a rate equation model, leading to the following differential equation system:

$$\frac{d}{dt} \begin{pmatrix} n_g \\ n_m \\ n_h \\ n_e \end{pmatrix} = \begin{pmatrix} -R & \Gamma_{mg} & \Gamma_{hg} & R + \Gamma_{eg} - W_{CR} \\ 0 & -\Gamma_{mg} & \Gamma_{hm} & \Gamma_{em} + 2W_{CR} \\ 0 & 0 & -\Gamma_{hm} - \Gamma_{hg} & \Gamma_{eh} \\ R & 0 & 0 & -R - \Gamma_{em} - \Gamma_{eg} - \Gamma_{eh} - W_{CR} \end{pmatrix} \begin{pmatrix} n_g \\ n_m \\ n_h \\ n_e \end{pmatrix} \quad (B1)$$

and the populations verify  $n_g + n_m + n_h + n_e = 1$ . The notations are as follows:  $\Gamma_{ij}$  is the total relaxation rate from level  $i$  to  $j$ , including radiative and non-radiative channels.  $W_{CR}$  is the concentration-dependent cross-relaxation rate. Solving this differential system yields the time- and space-dependent atomic populations in all four levels.

Given the pumping rate  $R = 340 s^{-1}$  at the center of the pumping beam and duration  $T_P = 3$  ms, we consider the population to be linearly depending on the laser power (perturbative population change since  $RT_P \lesssim 1$ ). Consequently the atomic populations have independent time and space dependence so they can be written as the product of two separable functions. With this we write the metastable population as:  $n_m(x, y, t) = n_m(x, y, T_P)g_m(t)$  where  $g_m(t) = \frac{n_m(0,0,t)}{n_m(0,0,T_P)}$ .

## Appendix C: Phonon-driven heatload

The total heatload power due to phonon emission is the sum of four terms:

$$P_{\text{heat}}(t) = N_{\text{Tm}}(P_{CR} + P_{eh} + P_{hm} + P_{mg}) \quad (C1)$$

where  $N_{\text{Tm}}$  is the number of atoms in the illuminated volume. Each term of the sum can be expressed in terms of atomic populations:

$$\begin{aligned} P_{CR} &= W_{CR} \Delta_{CR} n_e(t) \\ P_{eh} &= \Gamma_{eh}^{NR} \Delta_{eh} n_e(t) \\ P_{hm} &= \Gamma_{hm}^{NR} \Delta_{hm} n_h(t) \\ P_{mg} &= \Gamma_{mg}^{NR} \Delta_{mg} n_m(t) \end{aligned} \quad (C2)$$

$$(C3)$$

where  $\Delta_{CR}$  is the detuning between the two transitions involved in the cross-relaxation process,  $\Delta_{ij}$  is the energy

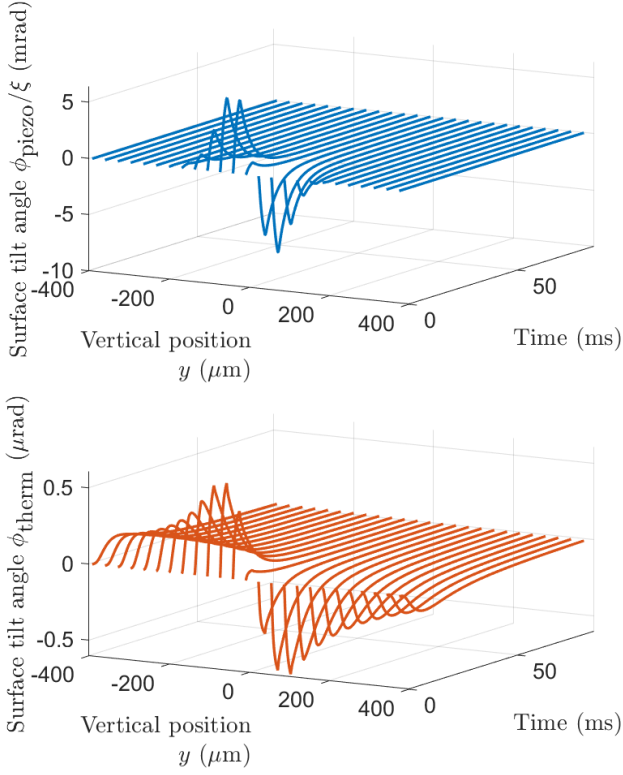


FIG. 12. Deflection angles  $\phi(y, t)$  derived from our piezoscopic and photothermal models, including the effect of the probe beam gaussian profile.

splitting between levels  $i$  and  $j$ .  $\Gamma_{ij}^{NR}$  is the non-radiative part of the relaxation rate along transition  $i \rightarrow j$ .

We do not include radiation trapping [65] for photons radiated from the metastable state, because this mechanism occurs in the whole crystal volume, given the moderate absorption coefficient along the  $g \rightarrow m$  transition [41].

#### Appendix D: Heat equation

Given the problem geometry, we write the heat equation in cylindrical coordinates, assuming a complete translational invariance along the cylinder axis (laser beam) as a simplification, and rotational invariance around its axis:

$$\frac{\partial T}{\partial t} = \alpha \frac{1}{r} \frac{\partial}{\partial r} \left( r \frac{\partial T}{\partial r} \right) + \frac{q(r, t)}{\rho c_p} \quad (\text{D1})$$

The cylinder is assumed to have infinite length. The temperature at the start of the pumping pulse is assumed uniform and equal to zero. The source term  $q(r, t)$  is the time- and space-dependent volumetric heatload. It is derived from  $P_{\text{heat}}$ , taking into account the gaussian profile of the pump beam.

The presence of the nearby surface alters the heat diffusion mechanism. Indeed, the low air conductivity imposes a zero heat flow through the surface. To account for this boundary condition we make the problem symmetric by assuming a second identical cylindrical heat source inside the infinite crystal centered at position  $(D_0, 0)$ .

#### Appendix E: Modeled photodeflection signal

From the calculated surface displacements presented in Figure 9 we obtain the expected surface tilt angles  $\phi_{\text{piezo}}(y, t)$  and  $\phi_{\text{therm}}(y, t)$  by a time derivation. To account for the finite size of the probe beam on the surface, we convolve the simulated angles with the gaussian profile of the probe beam. The results are shown in Figure 12. Again, the photothermal effect reveals the diffusion process inherent to heating mechanisms, whereas the piezoscopic contribution is more localized spatially and directly reflects the evolution of the metastable state population.

#### Appendix F: Macroscopic estimation of the piezoscopic effect magnitude

The magnitude of the piezoscopic effect is fundamentally related to the pressure sensitivity of an atomic line  $G_{\text{stress}} = \frac{\partial \omega}{\partial \sigma}$ , expressed in Hz/Pa. We consider the mechanical system made of a  $d_x \times d_y \times d_z$  rectangular cuboid (see Figure 13). The piezoscopic effect of  $N$  active ions within this volume creates a pressure  $\sigma$  on the  $yz$  surface that we can relate to the expansion  $\Delta x$  along the  $x$  dimension via Hooke's law:

$$\sigma = E \frac{\Delta x}{d_x} \quad (\text{F1})$$

where  $E$  is the Young modulus of the medium. The conservative force  $F = \sigma d_y d_z$  resulting from this pressure in the  $x$  direction can also be written as the spatial derivative of the  $N$  excited ions internal energy and undergoing the volumic change [66]:

$$F = \frac{\partial}{\partial x} (N \hbar \omega) = N \hbar \frac{\partial \omega}{\partial x} \quad (\text{F2})$$

The factor  $\frac{\partial \omega}{\partial x}$  is the atomic line sensitivity to a displacement of the  $yz$  surface. Again, using Hooke's law, we obtain

$$F = N \hbar \frac{E}{d_x} G_{\text{stress}} \quad (\text{F3})$$

$N$  is the total number of Tm ions in the volume:  $N = n_{\text{Tm}} d_x d_y d_z n_{\text{active}}$ , where  $n_{\text{active}}$  is the fraction of ions in the volume that generate the volumic change. Relating pressure and force (equations F1 and F3) we obtain:

$$\Delta x = \hbar G_{\text{stress}} n_{\text{active}} n_{\text{Tm}} d_x \quad (\text{F4})$$

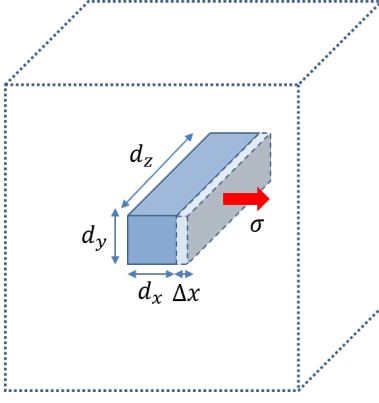


FIG. 13. Notations used for the macroscopic estimation of the piezoscopic magnitude (Appendix F).

- 
- [1] P. Treutlein, C. Genes, K. Hammerer, M. Poggio, and P. Rabl, Hybrid mechanical systems, in *Cavity Optomechanics* (Springer, 2014) pp. 327–351.
  - [2] J. J. Viennot, X. Ma, and K. W. Lehnert, Phonon-number-sensitive electromechanics, *Phys. Rev. Lett.* **121**, 183601 (2018).
  - [3] P. Treutlein, D. Hunger, S. Camerer, T. W. Hänsch, and J. Reichel, Bose-Einstein condensate coupled to a nanomechanical resonator on an atom chip, *Phys. Rev. Lett.* **99**, 140403 (2007).
  - [4] O. Arcizet, V. Jacques, A. Siria, P. Poncharal, P. Vincent, and S. Seidelin, A single nitrogen-vacancy defect coupled to a nanomechanical oscillator, *Nat. Phys.* **7**, 879 (2011).
  - [5] I. Yeo, P.-L. de Assis, A. Gloppe, E. Dupont-Ferrier, P. Verlot, N. S. Malik, E. Dupuy, J. Claudon, J.-M. Gérard, A. Auffèves, *et al.*, Strain-mediated coupling in a quantum dot–mechanical oscillator hybrid system, *Nat. Nanotechnol.* **9**, 106 (2014).
  - [6] J. Teissier, A. Barfuss, P. Appel, E. Neu, and P. Maletinsky, Strain coupling of a nitrogen-vacancy center spin to a diamond mechanical oscillator, *Phys. Rev. Lett.* **113**, 020503 (2014).
  - [7] P. Ouartchaiyapong, K. W. Lee, B. A. Myers, and A. C. B. Jayich, Dynamic strain-mediated coupling of a single diamond spin to a mechanical resonator, *Nat. Commun.* **5**, 1 (2014).
  - [8] K. Hammerer, K. Stannigel, C. Genes, P. Zoller, P. Treutlein, S. Camerer, D. Hunger, and T. W. Hänsch, Optical lattices with micromechanical mirrors, *Phys. Rev. A* **82**, 021803 (2010).
  - [9] K. Mølmer, Y. Le Coq, and S. Seidelin, Dispersive coupling between light and a rare-earth-ion-doped mechanical resonator, *Phys. Rev. A* **94**, 053804 (2016).
  - [10] R. Ohta, L. Herpin, V. M. Bastidas, T. Tawara, H. Yamaguchi, and H. Okamoto, Rare-earth-mediated optomechanical system in the reversed dissipation regime, *Phys. Rev. Letters* **126**, 047404 (2021).
  - [11] D. Tumanov, N. Vaish, H. A. Nguyen, Y. Curé, J.-M. Gérard, J. Claudon, F. Donatini, and J.-P. Poizat, Static strain tuning of quantum dots embedded in a photonic wire, *Appl. Phys. Lett.* **112**, 123102 (2018).
  - [12] N. Galland, N. Lučić, B. Fang, S. Zhang, R. Le Targat, A. Ferrier, P. Goldner, S. Seidelin, and Y. Le Coq, Mechanical tunability of an ultranarrow spectral feature of a rare-earth-doped crystal via uniaxial stress, *Phys. Rev. Appl.* **13**, 044022 (2020).
  - [13] M. W. Doherty, V. V. Struzhkin, D. A. Simpson, L. P. McGuinness, Y. Meng, A. Stacey, T. J. Karle, R. J. Hemley, N. B. Manson, L. C. Hollenberg, *et al.*, Electronic properties and metrology applications of the diamond NV-center under pressure, *Phys. Rev. Lett.* **112**, 047601 (2014).
  - [14] J. He and D. R. Clarke, Determination of the piezoelectroscopic coefficients for chromium-doped sapphire, *J. Am. Ceram. Soc.* **78**, 1347 (1995).
  - [15] S. Rajendran, N. Zobrist, A. O. Sushkov, R. Walsworth, and M. Lukin, A method for directional detection of dark matter using spectroscopy of crystal defects, *Phys. Rev. D* **96**, 035009 (2017).
  - [16] A. Louchet-Chauvet, R. Ahlefeldt, and T. Chanelière, Piezospectroscopic measurement of high-frequency vibrations in a pulse-tube cryostat, *Rev. Sci. Instrum.* **90**, 034901 (2019).
  - [17] F. J. Schüle, E. Zallo, P. Atkinson, O. G. Schmidt, R. Trotta, A. Rastelli, A. Wixforth, and H. J. Krenner, Fourier synthesis of radiofrequency nanomechanical pulses with different shapes, *Nat. Nanotechnol.* **10**, 512 (2015).
  - [18] J. Kettler, N. Vaish, L. M. de Lépinay, B. Besga, P.-L. de Assis, O. Bourgeois, A. Auffèves, M. Richard, J. Claudon, J.-M. Gérard, *et al.*, Inducing micromechanical motion by optical excitation of a single quantum dot, *Nat. Nanotechnol.* **16**, 283 (2021).
  - [19] C. Fabre, M. Gross, J. Raimond, and S. Haroche, Measuring atomic dimensions by transmission of Rydberg atoms through micrometre size slits, *J. Phys. B* **16**, L671 (1983).
  - [20] C. H. Metzger and K. Karrai, Cavity cooling of a microlever, *Nature* **432**, 1002 (2004).
  - [21] S. Gigan, H. R. Böhm, M. Paternostro, F. Blaser, G. Langer, J. B. Hertzberg, K. C. Schwab, D. Bäuerle, M. Aspelmeyer, and A. Zeilinger, Self-cooling of a micromirror by radiation pressure, *Nature* **444**, 67 (2006).

- [22] H. Ren, M. H. Matheny, G. S. MacCabe, J. Luo, H. Pfeifer, M. Mirhosseini, and O. Painter, Two-dimensional optomechanical crystal cavity with high quantum cooperativity, *Nat. Commun.* **11**, 1 (2020).
- [23] T. Briant, P.-F. Cohadon, M. Pinard, and A. Heidmann, Optical phase-space reconstruction of mirror motion at the attometer level, *Eur. Phys. J. D* **22**, 131 (2003).
- [24] Y. C. Sun, Rare earth materials in optical storage and data processing applications, in *Spectroscopic properties of rare earths in optical materials* (Springer, 2005) pp. 379–429.
- [25] I. Usmani, M. Afzelius, H. De Riedmatten, and N. Gisin, Mapping multiple photonic qubits into and out of one solid-state atomic ensemble, *Nat. Commun.* **1**, 1 (2010).
- [26] M. J. Thorpe, L. Rippe, T. M. Fortier, M. S. Kirchner, and T. Rosenband, Frequency stabilization to  $6 \times 10^{-16}$  via spectral-hole burning, *Nat. Photonics* **5**, 688 (2011).
- [27] X. Fernandez-Gonzalvo, Y.-H. Chen, C. Yin, S. Rogge, and J. J. Longdell, Coherent frequency up-conversion of microwaves to the optical telecommunications band in an Er:YSO crystal, *Phys. Rev. A* **92**, 062313 (2015).
- [28] A. Kinoshita, D. Hunger, R. Kolesov, K. Mølmer, H. de Riedmatten, P. Goldner, A. Tallaie, L. Morvan, P. Berger, S. Welinski, *et al.*, Roadmap for rare-earth quantum computing, arXiv preprint arXiv:2103.15743 (2021).
- [29] R. M. Macfarlane, Photon-echo measurements on the trivalent thulium ion, *Opt. Lett.* **18**, 1958 (1993).
- [30] A. Louchet, J. S. Habib, V. Crozatier, I. Lorgeré, F. Goldfarb, F. Bretenaker, J.-L. Le Gouët, O. Guillot-Noël, and P. Goldner, Branching ratio measurement of a  $\Lambda$  system in  $\text{Tm}^{3+}$ :YAG under a magnetic field, *Phys. Rev. B* **75**, 035131 (2007).
- [31] T. Chanelière, M. Bonarota, V. Damon, R. Lauro, J. Ruggiero, I. Lorgeré, and J.-L. Le Gouët, Light storage protocols in  $\text{Tm}$ :YAG, *J. Lumin.* **130**, 1572 (2010).
- [32] V. Damon, M. Bonarota, A. Louchet-Chauvet, T. Chanelière, and J.-L. Le Gouët, Revival of silenced echo and quantum memory for light, *New J. Phys.* **13**, 093031 (2011).
- [33] W. R. Babbitt, Z. W. Barber, S. H. Bekker, M. D. Chase, C. Harrington, K. D. Merkel, R. K. Mohan, T. Sharpe, C. R. Stiffler, A. S. Traxinger, *et al.*, From spectral holeburning memory to spatial-spectral microwave signal processing, *Laser Phys.* **24**, 094002 (2014).
- [34] P. Berger, Y. Attal, M. Schwarz, S. Molin, A. Louchet-Chauvet, T. Chanelière, J.-L. Le Gouët, D. Dolfi, and L. Morvan, RF spectrum analyzer for pulsed signals: ultra-wide instantaneous bandwidth, high sensitivity, and high time-resolution, *J. Light. Technol.* **34**, 4658 (2016).
- [35] L. Ulrich, P. Berger, A. Louchet-Chauvet, J. de Rosny, and L. Morvan, High rejection and frequency tunable optical filtering of RF signals using a rare earth ion-doped crystal (2021), in preparation.
- [36] K. B. Keating and H. G. Drickamer, Effect of pressure on the spectra of rare earth ions in crystals, *J. Chem. Phys.* **34**, 143 (1961).
- [37] E. Rodríguez, J. O. Tocho, and F. Cussó, Simultaneous multiple-wavelength photoacoustic and luminescence experiments: A method for fluorescent-quantum-efficiency determination, *Phys. Rev. B* **47**, 14049 (1993).
- [38] M. Grinberg, A. Sikorska, and S. Kaczmarek, Photoacoustic spectroscopy of YAG crystals doped with Ce, *Journal of Alloys and Compounds* **300**, 158 (2000).
- [39] R. Moncorgé, Current topics in rare-earth lasers, in *Spectroscopic properties of rare earths in optical materials* (Springer, 2005) pp. 320–378.
- [40] J. Caird, L. DeShazer, and J. Nella, Characteristics of room-temperature  $2.3\text{-}\mu\text{m}$  laser emission from  $\text{Tm}^{3+}$  in YAG and  $\text{YAlO}_3$ , *IEEE J. Quantum Electron.* **11**, 874 (1975).
- [41] R. C. Stoneman and L. Esterowitz, Efficient, broadly tunable, laser-pumped  $\text{Tm}$ :YAG and  $\text{Tm}$ :YSGG cw lasers, *Opt. Lett.* **15**, 486 (1990).
- [42] C. D. Brandle, Czochralski growth of oxides, *J. Cryst. Growth* **264**, 593 (2004).
- [43]  $\text{Tm}$ :YAG absorption chart, [https://www.scientificmaterials.com/downloads/Tm\\_YAG.pdf](https://www.scientificmaterials.com/downloads/Tm_YAG.pdf), accessed: 2021-04-20.
- [44] G. Armagan, A. M. Buoncristiani, and B. Di Bartolo, Excited state dynamics of thulium ions in yttrium aluminum garnets, *Opt. Mater.* **1**, 11 (1992).
- [45] A. C. Tam, Applications of photoacoustic sensing techniques, *Rev. Mod. Phys.* **58**, 381 (1986).
- [46] M. A. Olmstead, N. M. Amer, S. Kohn, D. Fournier, and A. C. Boccara, Photothermal displacement spectroscopy: an optical probe for solids and surfaces, *Appl. Phys. A* **32**, 141 (1983).
- [47] R. D. Shannon, Revised effective ionic radii and systematic studies of interatomic distances in halides and chalcogenides, *Acta Cryst. A* **32**, 751 (1976).
- [48] P. H. Klein and W. J. Croft, Thermal conductivity, diffusivity, and expansion of  $\text{Y}_2\text{O}_3$ ,  $\text{Y}_3\text{Al}_5\text{O}_{12}$ , and  $\text{LaF}_3$  in the range 77–300 K, *J. Appl. Phys.* **38**, 1603 (1967).
- [49] A. J. Freeman and R. E. Watson, Theoretical investigation of some magnetic and spectroscopic properties of rare-earth ions, *Phys. Rev.* **127**, 2058 (1962).
- [50] B. G. Wybourne and L. Smentek, *Optical spectroscopy of lanthanides: magnetic and hyperfine interactions* (CRC press, 2007).
- [51] K. Usami, A. Naesby, T. Bagci, B. M. Nielsen, J. Liu, S. Stobbe, P. Lodahl, and E. S. Polzik, Optical cavity cooling of mechanical modes of a semiconductor nanomembrane, *Nature Physics* **8**, 168 (2012).
- [52] A. Niguès, A. Siria, and P. Verlot, Dynamical backaction cooling with free electrons, *Nature communications* **6**, 1 (2015).
- [53] J. J. Longdell and M. J. Sellars, Experimental demonstration of quantum-state tomography and qubit-qubit interactions for rare-earth-metal-ion-based solid-state qubits, *Phys. Rev. A* **69**, 032307 (2004).
- [54] L. Rippe, B. Julsgaard, A. Walther, Y. Ying, and S. Kröll, Experimental quantum-state tomography of a solid-state qubit, *Physical Review A* **77**, 022307 (2008).
- [55] M. Nilsson, L. Rippe, S. Kröll, R. Klieber, and D. Suter, Hole-burning techniques for isolation and study of individual hyperfine transitions in inhomogeneously broadened solids demonstrated in  $\text{Pr}^{3+}:\text{Y}_2\text{SiO}_5$ , *Physical Review B* **70**, 214116 (2004).
- [56] W. Tittel, M. Afzelius, R. Cone, T. Chanelière, S. Kröll, S. Moiseev, and M. Sellars, Photon-echo quantum memory in solid state systems, *Laser Photonics Reviews* **4**, 244 (2010).
- [57] T. Chanelière, G. Hétet, and N. Sangouard, Quantum optical memory protocols in atomic ensembles, *Advances In Atomic, Molecular, and Optical Physics* **67**, 77 (2018).
- [58] T. Lutz, L. Veissier, C. W. Thiel, R. L. Cone, P. E. Barclay, and W. Tittel, Modification of phonon processes

- in nanostructured rare-earth-ion-doped crystals, *Physical Review A* **94**, 013801 (2016).
- [59] A. Clerk, K. Lehnert, P. Bertet, J. Petta, and Y. Nakamura, Hybrid quantum systems with circuit quantum electrodynamics, *Nature Physics* **16**, 257 (2020).
  - [60] G. Cittadino, A. Volpi, A. Di Lieto, and M. Tonelli, Codoping of  $\text{LiYF}_4$  crystal: a virtuous effect of cooling efficiency, *Journal of Physics D: Applied Physics* **51**, 145302 (2018).
  - [61] Z. Zhang, A. Louchet-Chauvet, L. Morvan, P. Berger, P. Goldner, and A. Ferrier, Tailoring the  $^3\text{F}_4$  level lifetime in  $\text{Tm}^{3+}:\text{Y}_3\text{Al}_5\text{O}_{12}$  by  $\text{Eu}^{3+}$  co-doping for signal processing application, *J. Lumin.* **222**, 117107 (2020).
  - [62] S. D. Melgaard, A. R. Albrecht, M. P. Hehlen, and M. Sheik-Bahae, Solid-state optical refrigeration to sub-100 kelvin regime, *Scientific reports* **6**, 1 (2016).
  - [63] R. Vicente, G. Nogues, L. Del-Rey, J. Debray, D. Jegouso, J.-F. Motte, G. Cittadino, A. Di Lieto, M. Tonelli, J.-M. Niot, and A. Gardelein, Demonstration of a fiber-coupled optical cryocooler: a step towards future space applications, in *Photonic Heat Engines: Science and Applications III*, Vol. 11702, edited by D. V. Seletskiy, M. Sheik-Bahae, and M. K. Kuno, International Society for Optics and Photonics (SPIE, 2021).
  - [64] L. Guillemot, P. Loiko, E. Kifle, J.-L. Doualan, A. Braud, F. Starecki, T. Georges, J. Rouvillain, A. Hideur, and P. Camy, Watt-level mid-infrared continuous-wave Tm:YAG laser operating on the  $^3\text{H}_4 \rightarrow ^3\text{H}_5$  transition, *Opt. Mater.* **101**, 109745 (2020).
  - [65] A. F. Molisch and B. P. Oehry, *Radiation trapping in atomic vapours* (Oxford University Press, 1998).
  - [66] J. Leech, *Classical Mechanics* (Methuen & co, 1965).